Hydrodynamic force induced by vortex–body interactions in orderly formations of flapping tandem flexible plates

Linlin Kang (康林林), Weicheng Cui (崔维成), Xi-Yun Lu (陆夕云), et al.

View Online **Export Citation** **CrossMark**

ARTICLES YOU MAY BE INTERESTED IN

Intermittent swimming of two self-propelled flapping plates in tandem configuration
Physics of Fluids **34**, 011905 (2022); https://doi.org/10.1063/5.0078829

Hydrodynamic analysis of fish schools arranged in the vertical plane
Physics of Fluids **33**, 121905 (2021); https://doi.org/10.1063/5.0073728

Active external control effect on the collective locomotion of two tandem self-propelled flapping plates
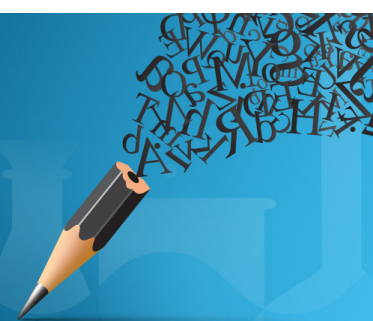Physics of Fluids **33**, 101901 (2021); https://doi.org/10.1063/5.0065256

Hydrodynamic force induced by vortex–body interactions in orderly formations of flapping tandem flexible plates

View Online   Export Citation   CrossMark

Linlin Kang (康林林),[1,a] (ID) Weicheng Cui (崔维成),[1,a] (ID) Xi-Yun Lu (陆夕云),[2] (ID) and Haibo Huang (黄海波)[2,b] (ID)

AFFILIATIONS

[1] Key Laboratory of Coastal Environment and Resources of Zhejiang Province (KLaCER), School of Engineering, Westlake University, Hangzhou 310024, Zhejiang, China
[2] Department of Modern Mechanics, University of Science and Technology of China, Hefei 230026, Anhui, China

[a] **Present address:** Institute of Advanced Technology, Westlake Institute for Advanced Study, Hangzhou 310024, Zhejiang, China.
[b] **Author to whom correspondence should be addressed:** huanghb@ustc.edu.cn

ABSTRACT

The mechanism behind stable aggregations of active swimmers is not fully understood. In particular, the in-depth quantitative explanations are notably lacking. To address this, a vorticity-based force expression is proposed to study the collective behaviors of two two-dimensional tandem flapping plates. The hydrodynamic force is directly related to the generation of vorticity on the plate and viscous forces resulting from its subsequent evolution. For the first time, the physical process by which the interactions between the rear plate and the wake vortices of the leader affects the hydrodynamic force is quantitatively elucidated and not based on simplified theory. The wake vortices of the leader influence the hydrodynamic force on the rear plate indirectly by inducing an additional oncoming flow. The flow affects the generation of vorticity, which mainly occurs on the head of the rear plate. The results show that, if the trajectory of the rear plate passes through the vortex cores, vorticity generation on the rear plate is suppressed and the thrust effect is weakened. If the rear plate slaloms between the vortices, the vorticity generation and the thrust effect are enhanced. We also found that the wake vortices of the leader has a certain ability to trap the rear plate into orderly configurations—no matter the rear plate has a dissimilar flapping amplitude or is applied an external horizontal loading—by adjusting the equilibrium position of the rear plate in it. The findings may shed some light on the understanding of collective behaviors in swimming animals.

I. INTRODUCTION

Fish schools and flying formations are fascinating examples of collective behaviors in nature. Although there are numerous studies on fish schools and bird flocks,[1–5] the mechanism behind the orderly formation of aggregation remains unclear.[6] It is well known that an individual in the groups may encounter complex vortices shedding from surrounding individuals. Vortex–body interactions are important. After a variety of experimental observations and numerical simulations, there is a common perception that energy extraction from environmental vortices is important to enhance the performance of collective locomotion.[2,5–16] However, quantitative information is limited because of the difficulty in measurement and lack of vorticity-based theories.

The classic explanation for orderly formations is that each individual adopts an optimal position to form a constructive interaction with the environmental vorticity.[2] Weihs believed that a diamond configuration is energetically optimal for fish schooling. In recent studies, other configurations are also found to show hydrodynamic advantages.[11,12,17] Thus, the optimal configuration in fish schools, in particular, the underlying physical mechanism, remains controversial. An important question arises whether the emergence of the stable configuration is due to passive forces or elaborate control mechanisms. Lighthill conjectured that for sufficiently fast locomotion, the orderly formations may arise passively from the hydrodynamic interactions without elaborate control,[18] which is called *Lighthill conjecture*.[13,19,20]

A two-body system is the simplest model to investigate the collective behavior and the conjecture. Flow-mediated interactions between two passively flapping filaments or flags in a flow[8,21–23] as well as two actively flapping bodies[24–27] were studied. In these studies, the streamwise locations of the wings or foils were fixed. Their results show that

the vortices shed by the front body interact with the rear one, which leads to different propulsive performances of the rear one.[26,28,29] However, there is no quantitative analysis of how the hydrodynamic force of the rear plate depending on the interaction.

In addition to the above fixed flapping model, self-propelled flapping models were proposed to study the *Lighthill conjecture*.[6,13,17,19,20,30–33] These models are more realistic because each individual in the group is free to select its propulsion speed and equilibrium streamwise location. The studies of these self-propelled models show that multiple stable configurations may emerge passively from vortex–body interactions.[17] Zhu *et al.*[6] observed that the rear plate's trajectory is locked onto the vortex centers. They proposed a hypothesized mechanism for the behavior, i.e., in this way the rear plate can obtain energetic benefits by moving with the local lateral flow rather than against it. However, the *vortex locking* behavior is not the only choice of vortex–body interaction for orderly formations of tandem configuration.[7,34] Ramananarivo *et al.*[13] found that in stable configurations, when the rear foil is perturbed slightly, it will robustly return to its equilibrium location. It seems that the rear foil experiences a spring-like restoring force. To explain it, an interaction potential is constructed, in which the stable wells in an energy landscape correspond to the observed equilibrium locations of the rear plate. Park and Sung[17] found four stable configurations (tandem, diagonal, triangular, and diamond) for schools with more individuals and the effect of vortex–body interactions on the propulsive performance was investigated qualitatively. Newbolt *et al.*[31] found that two foils with different flapping motions swimming in tandem can also form stable configurations, and the interaction of the follower with the vortex wake left by the leader was analyzed by a simplified velocity-based model.

To quantitatively clarify the effect of vortex–body interaction, vorticity-based representations and interpretations are required. There are several classical vorticity-based theories or models used for the collective locomotion dynamics, such as Wu's linear (small-amplitude) theory,[35,36] the linear unsteady airfoil theory,[37,38] and some extension models.[13,39,40] In the theoretical analysis of the vortex–body interaction, a vortex sheet model, or a point vortex model, or the undistributed vortex street past an oscillating foil may be adopted. To some extent, these theories shed some light on the mechanism for the stable positioning of the rear body. On the other hand, in the theories, the assumptions of small flapping amplitude, zero foil thickness, potential flow, negligible nonlinear terms, or viscosity, etc. do not exactly match the real situation. In addition, the theories are not able to describe the physical process of vortex generation and shedding from the surface of the rear body.

Due to advances in the experimental technique and numerical simulation, it is possible to quantify the instantaneous vortex structures and interpret the vortex–body interaction under a theoretical, vorticity-based framework. The impulse theory proposed by Wu[41] provides the relationship between the force and the change rate of vorticity moment in viscous flow. Despite its generality and neatness, the theory has an inherent limitation that requires calculating the entire vorticity field. Recently, a two-dimensional potential flow model in terms of impulse theory has been proposed and a fruitful separation of the main contributions due to added mass and to vorticity release is obtained by decomposing the impulse into potential impulse and vortical impulse.[42,43] The extension of this model to viscous flow is significant. Some recent studies show that there is no obvious one-to-one connection between the swimming performance (thrust, power, and efficiency) and the details of the wake structure.[44] Therefore, the wake structures and the propulsion performance should be treated as two separate but inter-related topics. The hydrodynamic force exerted on a self-propelled body is dominated by the local dynamic processes and flow structures generated by the body motion. To quantify the effects of local processes and structures, some unconventional vorticity-based force expressions are proposed,[45,46] which provide better insights into local dynamics. Furthermore, inspired by the work of Li and Lu,[47] Kang *et al.*[48] proposed a minimum-domain impulse theory. Using the theory, the entire force on the body can be completely determined by only the time rate of the impulse of those vortical structures still connecting to the body, along with the Lamb-vector integral thereof.

Based on our previous work,[48] here we further propose a quantitative derivation of vorticity-based force theory which directly relates the hydrodynamic force to the vorticity generation and evolution on the body surface. The purpose of this paper is to apply the proposed theory to quantitatively analyze the vortex–body interaction in viscous fluid. The cases of hydrodynamic schooling of two two-dimensional flapping flexible plates in tandem at low Reynolds number are considered. Different from previous numerical studies[6,20,34] focusing on the kinematic characteristics of collective motion (such as the gap spacing and propulsive performance of the collective system), this paper pays more attention to its dynamic characteristics and quantitative interpretation of the influence of vortex–plate interaction on its force characteristics, and further elucidates the underlying mechanism of spontaneous formation of ordered configurations.

The outline of the paper is as follows. The physical problem and numerical method are described in Sec. II. The force expressions in terms of local vortical structures are given in Sec. III. The emergent configurations and the correlation between hydrodynamic force and vortex–body interactions are discussed in Sec. IV. In this section, the hydrodynamic force on the plate is quantitatively analyzed in the vorticity-based frame in terms of instantaneous flow structures. By changing the flapping amplitude of the rear plate or applying external loading on it, we study how stable the configuration is. Finally, concluding remarks are addressed in Sec. V.

II. PHYSICAL PROBLEM AND NUMERICAL METHOD

As shown in Fig. 1, two flapping flexible plates in tandem with length L are driven at the leading edge by harmonic plunging motions of amplitude a_i ($i = 1, 2$) and frequency f in a two-dimensional stationary viscous incompressible fluid. The forced lateral motions of the leading edges are described by

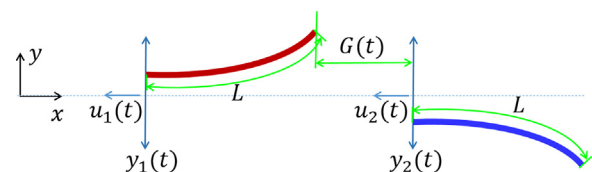$$y_1(t) = a_1 \cos(2\pi f t), \quad y_2(t) = a_2 \cos(2\pi f t - \Delta\phi), \quad (1)$$

FIG. 1. Schematic diagram of the two two-dimensional self-propelled plates driven by plunging motions $y_i(t)$ ($i = 1, 2$) in a tandem configuration. $G(t)$ is the gap spacing between the two plates. $u_i(t)$ is the streamwise velocity of the leading edge of the ith plate. L is the length of the plates.

where the subscripts 1 and 2 denote the front and rear plates, respectively; $\Delta\phi$ is the phase lag of the rear plate relative to the front plate. $u_i(t)$ is the streamwise velocity of the leading edge of the ith plate.

To identify the underlying mechanism of the stable configuration, the horizontal motions of the plates are set in three different forms: (i) the plates are free to move in the horizontal direction in a stationary fluid, as shown in Fig. 1, depending on the hydrodynamic force; (ii) the streamwise locations of the leading edges of the plates are fixed in the inertial coordinate system with a free oncoming flow; and (iii) an external horizontal load is applied to the self-propelled rear plate, which balances the net hydrodynamic force.

The fluid motion is described by the incompressible Navier–Stokes equations,

$$\nabla \cdot \boldsymbol{u} = 0, \tag{2}$$

$$\boldsymbol{a} = -\frac{1}{\rho}\nabla p + \frac{\mu}{\rho}\nabla^2 \boldsymbol{u} + \boldsymbol{f}, \tag{3}$$

where $\boldsymbol{u}$ is the velocity, $\boldsymbol{a} (= \partial\boldsymbol{u}/\partial t + \boldsymbol{u}\cdot\nabla\boldsymbol{u})$ the acceleration, p is the pressure, ρ is the density of fluid, and μ is the dynamic viscosity. $\boldsymbol{f}$ is the Eulerian force acting on fluid nodes.

The plates are assumed to be two-dimensional thin elastic beams, and their dynamics are governed by the nonlinear partial differential equation,[49]

$$\rho_s h \frac{\partial^2 \boldsymbol{X}}{\partial t^2} - \frac{\partial}{\partial s}\left[Eh\left(1 - \left|\frac{\partial \boldsymbol{X}}{\partial s}\right|^{-1}\right)\frac{\partial \boldsymbol{X}}{\partial s}\right] + EI\frac{\partial^4 \boldsymbol{X}}{\partial s^4} = \boldsymbol{F}_s, \tag{4}$$

where s is the Lagrangian coordinate along the plate, $\boldsymbol{X}$ is the position vector of the plate, $\rho_s h$ is the structural linear mass density, and Eh and EI are the stretching and bending rigidities of the plates, respectively. $\boldsymbol{F}_s$ is the Lagrangian force exerted on the plates by the surrounding fluid. In addition to satisfying Eq. (1), the leading edge of the plate satisfies boundary conditions $-Eh(1 - |\frac{\partial\boldsymbol{X}}{\partial s}|^{-1})\frac{\partial\boldsymbol{X}}{\partial s} + EI\frac{\partial^3\boldsymbol{X}}{\partial s^3} = \boldsymbol{0}$ and $\frac{\partial\boldsymbol{X}}{\partial s} = \boldsymbol{e}_x$, where $\boldsymbol{e}_x$ is the unit vector in the x direction. At the free trailing edge, we have $-Eh(1 - |\frac{\partial\boldsymbol{X}}{\partial s}|^{-1})\frac{\partial\boldsymbol{X}}{\partial s} + EI\frac{\partial^3\boldsymbol{X}}{\partial s^3} = 0, \frac{\partial^2\boldsymbol{X}}{\partial s^2} = \boldsymbol{0}$.

The reference quantities L, ρ, and U_{ref} are chosen to nondimensionalize the above mathematical formulation, where U_{ref} is the maximum flapping velocity of the plunging motion, i.e., $U_{ref} = 2\pi a_1 f$. The dimensionless parameters are defined as follows: the heaving amplitude $A_i = a_i/L$ for plate i, the flapping Reynolds number $Re_f = \rho U_{ref} L/\mu$, the bending stiffness $K = EI/\rho U_{ref}^2 L^3$, the stretching stiffness $S = Eh/\rho U_{ref}^2 L$, the mass ratio of the plates $M = \rho_l/\rho L$, and the gap spacing G/L. In the following descriptions, G denotes the normalized quantity G/L.

The Navier–Stokes equations are solved numerically by the lattice Boltzmann method (LBM).[51,52] It is known that in the direct numerical simulation of the incompressible Navier–Stokes equations, the pressure satisfies a Poisson equation with velocity strains acting as sources. Solving this equation for the pressure often produces numerical difficulties requiring special treatment, such as iteration or relaxation. In contrast, the incompressible Navier–Stokes equations can be obtained in the nearly incompressible limit of the LBM. The pressure of the LBM is calculated using an equation of state.[51] The deformation and motion of flexible plate are described by a structural equation which is solved by a finite element method in the Lagrange coordinate independently. For each plate, boundary conditions for the leading and trailing ends are

imposed. The movement of each plate (Lagrange points) is coupled with the LBM solver through an immersed boundary (IB) method,[53] which is used to enforce the no-slip boundary condition. The Lagrangian force $\boldsymbol{F}_s$ in Eq. (4) can be calculated by the feedback law,[53,55]

$$\boldsymbol{F}_s(s,t) = \alpha\int_0^t\left[\boldsymbol{u}_f(s,t') - \boldsymbol{u}_s(s,t')\right]dt' + \beta\left[\boldsymbol{u}_f(s,t) - \boldsymbol{u}_s(s,t)\right], \tag{5}$$

where α and β are free parameters and are selected based on Hua et al.[50] $\boldsymbol{u}_s = \partial\boldsymbol{X}/\partial t$ is the plate velocity, and the fluid velocity $\boldsymbol{u}_f$ at $\boldsymbol{X}$ is interpolated from the velocities of the surrounding fluid nodes $\boldsymbol{u}$, i.e.,

$$\boldsymbol{u}_f(s,t) = \int \boldsymbol{u}(\boldsymbol{x},t)\delta(\boldsymbol{x} - \boldsymbol{X}(s,t))d\boldsymbol{x}. \tag{6}$$

The body force $\boldsymbol{f}$ represents an Eulerian force on the fluid nodes, which are close to the moving wall boundary. It can be obtained from the Lagrangian force $\boldsymbol{F}_s$ using the Dirac δ function, i.e.,

$$\boldsymbol{f}(\boldsymbol{x},t) = -\int_L \boldsymbol{F}_s(\boldsymbol{X},t)\delta[\boldsymbol{x} - \boldsymbol{X}(s,t)]ds. \tag{7}$$

In our numerical simulation, a four-point regularized δ function is used,[53]

$$\delta_h = \frac{1}{\Delta x \Delta y}\phi\left(\frac{x}{\Delta x}\right)\phi\left(\frac{y}{\Delta y}\right), \tag{8}$$

where

$$\phi(r) = \begin{cases} \left(3 - 2|r| + \sqrt{1 + 4|r| - 4r^2}\right)/8, & |r| < 1, \\ \left(5 - 2|r| - \sqrt{-7 + 12|r| - 4r^2}\right)/8, & 1 \le |r| < 2, \\ 0, & |r| \ge 2, \end{cases} \tag{9}$$

where $|r|$ denotes the distance between the Lagrangian point and the nearby Eulerian grid points. See our previous work[34,50] for more details.

A finite moving computational domain is used in the x direction. As the plate travels one mesh spacing in the horizontal direction, the computational domain is shifted by adding one layer at the inlet and removing one layer at the outlet.[50] In the simulations, the Neumann boundary condition $\partial\boldsymbol{u}/\partial x = \boldsymbol{0}$ is applied at the outlet, and the Dirichlet boundary condition $\boldsymbol{u} = \boldsymbol{0}$ is applied at the inlet and other two boundaries.

Through convergence study, the computational domain is chosen as $45L \times 30L$ in the x and y directions. The mesh is uniform with spacing $\Delta x = \Delta y = 0.01L$. The time step is $\Delta t/T = 1/10\,000$ with $T = 1/f$ being the flapping period. To validate the numerical method in the present study, the locomotion of two self-propelled plates swimming in tandem is simulated with parameters $Re_f = 200$, $A = 0.5$, $M = 0.2$, $K = 0.8$, $S = 1000$. The parameters in the simulation are identical to those in Zhu et al.[6] and Peng et al.[20] Figure 2 shows the time history of the propulsion velocity (u_1) of the front plate. It is seen that the propulsion velocity of the front plate is consistent with those from Zhu et al.[6] and Peng et al.[20]

Grid independence and time step independence studies are also performed. The horizontal hydrodynamic force F_x and lateral
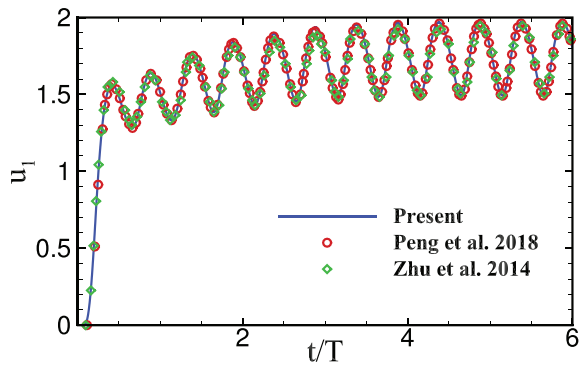
FIG. 2. Numerical validation. The time evolution of the propulsion velocity u_1 of the front plate. Line represents the present result. Symbols represent the results in Zhu et al.[6] and Peng et al.[20] In the case, the key parameters are: $Re_f = 200$, $A = 0.5$, $M = 0.2$, $K = 0.8$, $S = 1000$.

displacement y_{TE} of the rear plate in simulations with different mesh size and time step size are shown in Fig. 3. The propulsion velocities with different mesh size and time step size are shown in our previous work.[20] It is seen that $\Delta x/L = 0.01$ and $\Delta t/T = 0.0001$ are sufficient to achieve accurate results.

III. DYNAMIC EXPRESSIONS IN TERMS OF LOCAL FLOW STRUCTURES

To illustrate the dynamic expressions in terms of local flow structures, here we consider a typical external flow problem as shown in Fig. 4(a): a material body of volume B moves arbitrary in an incompressible viscous fluid. The body surface ∂B specifies velocity distribution $\boldsymbol{u} = \boldsymbol{u}_B$, where $\boldsymbol{u}$ and $\boldsymbol{u}_B$ are the velocity of the fluid and the velocity of the solid at the interface ∂B. For incompressible flow, the hydrodynamic force on the body B is expressed as

$$\boldsymbol{F}(t) = \int_{\partial B} (-p\boldsymbol{n} + \mu\boldsymbol{\omega} \times \boldsymbol{n})dS, \tag{10}$$

where p is the pressure, $\boldsymbol{\omega}\,(= \nabla \times \boldsymbol{u})$ the vorticity field, $\boldsymbol{n}$ the normal vector on ∂B pointing outside of domain B. From a physics perspective, the pressure is a noncompact physical variable which cannot directly relate the force on the body to the local flow structures

characterized by the environmental vortices.[48] It is a natural strategy to replace the pressure term in Eq. (10) with the function of vorticity.

As described in Sec. II, the effect of the flexible plate on the surrounding fluid can be replaced by the body force $\boldsymbol{f}$ in Eq. (19). Numerically, the body force can be obtained from the Lagrangian force $\boldsymbol{F}_s$ using a four-point regularized δ function.[50] Here, the force on the body is directly obtained by integrating the body force $\boldsymbol{f}$ of the flow field [see Fig. 4(b)], i.e.,

$$\boldsymbol{F}(t) = -\int_{V_{bf}} \rho\boldsymbol{f}dV, \tag{11}$$

where V_{bf} is the domain of the body force bounded by ∂V_{bf}. It is physically reasonable, and a similar strategy was used in discussion of impulse theory by Lighthill (Ref. 56, pp. 133–136). Substituting the hydrodynamic force with flow field variables, i.e., substituting Eq. (3) into Eq. (11), we have

$$\boldsymbol{F}(t) = -\int_{V_{bf}} \rho\boldsymbol{a}dV + \int_{\partial V_{bf}} (-p\boldsymbol{n} + \mu\boldsymbol{\omega} \times \boldsymbol{n})dS, \tag{12}$$

where the body force domain V_{bf} in our numerical simulation is shown in Fig. 4(c). To be consistent with the four-point regularized δ function, i.e., Eq. (8), the characteristic size of the domain of body force is chosen $R = 3\Delta x = 3\Delta y$. To confirm the validation of Eq. (12), the force on the flapping plate calculated by Eq. (12) is compared with the standard results which are calculated directly by the integral of the Lagrangian force $\boldsymbol{F}_s$ on the plate. From Fig. 5, it is seen that the hydrodynamic force (both F_x and F_y) on the plate can be well predicted by the integral of body force.

To interpret the vortex–body interaction as well as its induced hydrodynamic loading, a theoretical vorticity-based framework is needed. Although the minimum-domain impulse theory[48] is sufficiently concise in physics and form, it has a critical limitation, i.e., it is difficult to relate the hydrodynamic force to key physical process at different evolution stages. The limitation is due to the following reason. The impulse force term and the Lamb-vector integral term involved are distributed on the same flow structures and of equal order of magnitude. To solve this problem, here we develop a more concise expression in the following.

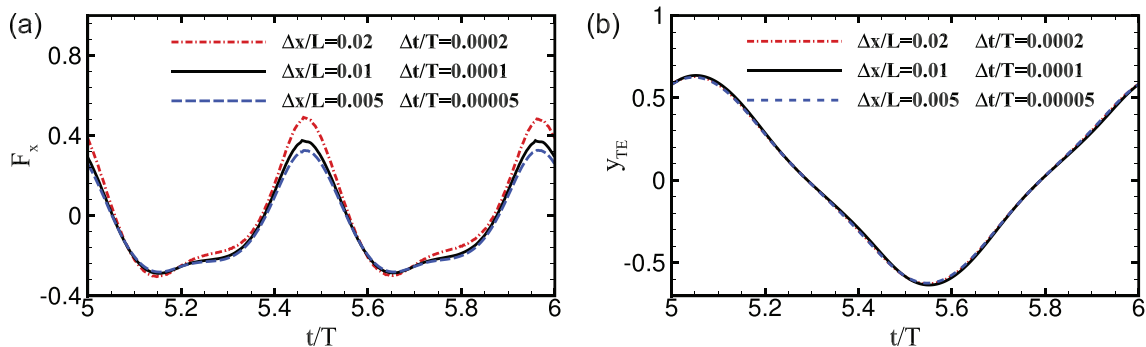For two-dimensional incompressible flow, the vorticity equation is

FIG. 3. The grid independence and time step independence studies for case with $Re_f = 200$, $A = 0.5$, $M = 0.2$, $K = 0.8$, $S = 1000$. The time evolution of (a) horizontal hydrodynamic force F_x and (b) the lateral displacement y_{TE} of the rear plate.
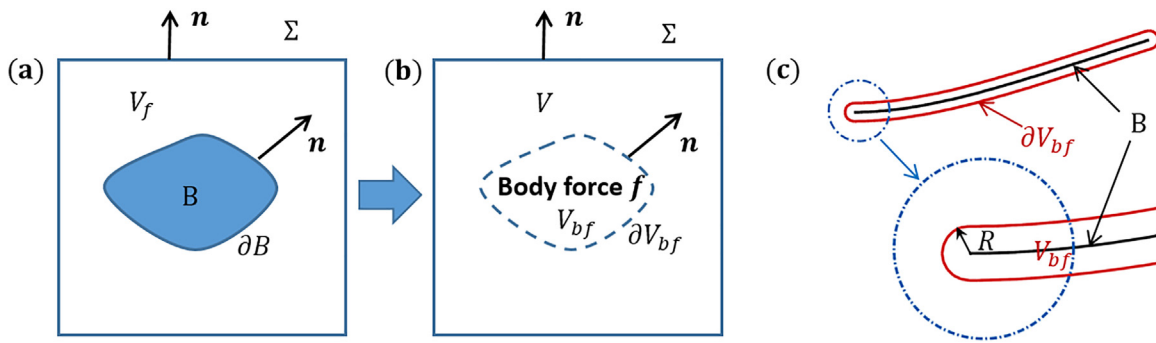
FIG. 4. (a) Schematic of a moving/deforming body through the fluid in an arbitrary control volume $V = V_f + B$ bounded by Σ. B is the domain of the body bounded by ∂B. V_f is the fluid domain. (b) The sketch of replacing the solid body B by an imaginary body force acting at the same domain of the body. V_{bf} is the domain of body force bounded by ∂V_{bf}. (c) The black solid line denotes the flapping plate. The domain of body force V_{bf} is bounded by the red solid line ($R = 3\Delta x = 3\Delta y$).

$$\frac{d\boldsymbol{\omega}}{dt} = \frac{\mu}{\rho}\nabla^2\boldsymbol{\omega} + \nabla \times \boldsymbol{f}, \tag{13}$$

and any V bounded by Σ as shown in Fig. 4(b) should satisfy $V \supseteq V_{bf}$, $\boldsymbol{f} = \boldsymbol{0}$ on Σ and outside Σ. By Eq. (A1), we have

$$\boldsymbol{F}(t) = -\int_V \rho \boldsymbol{f}\, dV = -\int_V \boldsymbol{x} \times (\nabla \times \rho \boldsymbol{f})\, dV, \tag{14}$$

where $\boldsymbol{x}$ is the position vector. Substituting Eq. (13) into Eq. (14), we can obtain

$$\begin{aligned}\boldsymbol{F} &= -\int_V \boldsymbol{x} \times \left[\frac{d(\rho\boldsymbol{\omega})}{dt} - \mu\nabla^2\boldsymbol{\omega}\right] dV, \\ &= -\int_V \boldsymbol{x} \times \frac{d(\rho\boldsymbol{\omega})}{dt}\, dV + \int_\Sigma \mu\boldsymbol{\omega} \times \boldsymbol{n}\, dS + \int_\Sigma \mu\boldsymbol{x} \times (\boldsymbol{n} \cdot \nabla\boldsymbol{\omega})\, dS,\end{aligned} \tag{15}$$

which directly relates the force to the evolution of vorticity in domain V as well as its viscous diffusion thereof. The latter can further be related to viscous friction and the boundary vorticity flux (Ref. 46, p. 125) on outer surface Σ. Since solid bodies are replaced by the body forces, and further replaced by vorticity terms using the vorticity equation, Eq. (15) can be used to solve the hydrodynamic force of multiple flapping plates and does not involve the domain connectivity issues. In Sec. IV, the performance of Eq. (15) in predicting the force on the plate
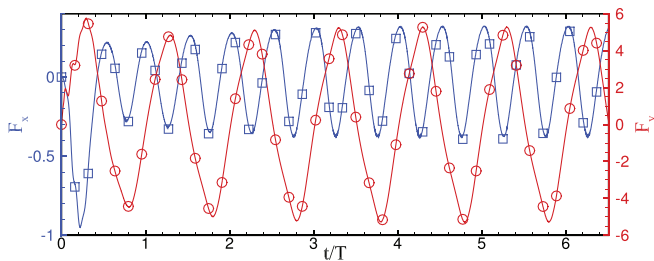
is discussed. It is worth mentioning that the impulse theory[48] can be obtained by substituting $\frac{d}{dt}\int_V \boldsymbol{x} \times \rho\boldsymbol{\omega}\, dV = \int_V \boldsymbol{x} \times \frac{d(\rho\boldsymbol{\omega})}{dt}\, dV - \int_V \rho\boldsymbol{\omega} \times \boldsymbol{u}\, dV + \int_\Sigma \boldsymbol{x} \times \rho\boldsymbol{\omega}(\boldsymbol{v} \cdot \boldsymbol{n})\, dS$, into Eq. (15), where $\boldsymbol{v}$ is the velocity of outer surface Σ.

Suppose the flow field consists of a set of discrete vortical structures, we can choose a special Σ to avoid cutting any discrete vortical structures, i.e., $\boldsymbol{\omega} = \boldsymbol{0}$ at and near Σ, then hydrodynamic force is all contributed by the first term on the right-hand side (RHS) of Eq. (15). More relevant discussion can be found in Kang et al.[48] Some recent studies show that the force on the body is not directly connected with the shed vortices,[44] but is related to the nearby vorticity directly.[48] In our simulation, the vorticity field can be approximated as discrete. To analyze the connection between force and vorticity, the strategy of Kang et al.[48] is adopted, i.e., the Σ cuts the vortices as small as possible and the domain V is chosen as small as possible. In this way, the hydrodynamic force, i.e., Eq. (15), especially its first term on the RHS would be further analyzed in Sec. IV.

For incompressible external flow problem, vorticity is generated at the boundary and is subsequently convected into the fluid and diffused. To further study the relation of the force to the generation of vorticity, the domain V is reduced to V_{bf} so Σ is replaced by the imaginary boundary of plate ∂V_{bf}. In this way, the first term on the RHS of Eq. (15) is associated with the generation of vorticity in the imaginary body V_{bf}. The second term on the RHS of Eq. (15) is the viscous force resulting from boundary vorticity flux. The third term is the viscous force, which is identical to the last term in Eq. (12).

IV. EMERGENT DYNAMICS AND FORCE LINKED TO VORTEX–BODY INTERACTIONS

In the current work, we focus on the underlying dynamic mechanisms behind the collective behavior of two self-propelled plates at low Reynolds number rather than systematically analyzing the effects of different parameters. The typical nondimensional parameters used in our simulations are $Re_f = 200$, $A = 0.5$, $M = 0.2$, $S = 1000$, and $K = 0.8$. To neglect the influence of the stretching deformation, the stretching stiffness of the plate S is chosen to be large enough. Usually, the bending stiffness of a fish is $K \sim O(1)$.[20] These parameters are identical to those in the "1A" case in Zhu et al.,[6] which is of the 2P wake mode; it means two pairs of vortices are shed within each flapping cycle. The investigation of Zhu et al.[6] indicates that the stable

FIG. 5. The evolution of the force on an isolate flapping plate with nondimensional parameters $Re = 200$, $A = 0.5$, $M = 0.2$, $S = 1000$. Solid lines and circle points denote the standard results calculated by the integral of $\boldsymbol{F}_s$ and the force calculated by Eq. (12), respectively.

configurations of two self-propelled flapping plates in tandem configuration can be categorized into a compact form and a regular form. In the compact form, the two plates are too close and the vortex–body analysis is not so clear as that in the regular form. Hence, in the present study, we focus on the regular form configuration to analyze the interplay among actuation, deformation and the vortical flow environment from the perspective of vortex dynamics. In the regular form, the stable gap spacing of two plates with identical flapping motions is an integer multiple of the wavelength traced out by the front plate, $\lambda = |U_e/f|$ $[U_e = \int_{tt}^{t/t+T} u_1(t)dt/T]$. In our cases, the Reynolds number referred to propulsion velocity is $Re_U = Re_f \cdot U_e \approx 352$. The Strouhal number, $St = A_{TE}f/U_e \approx 0.23$, is within the narrow range of St of real swimming animals,[54] where A_{TE} is the peak-to-peak flapping amplitude of the tail.

In the following, we first generally describe the effect of the wake vortices of the front plate on the propulsive performance of the rear plate by changing the flapping amplitude of the rear plate A_2 or the phase difference $\Delta\phi$ between the two plates; then we clarify how the reversed Kármán vortex street affects the force on the rear plate by vorticity dynamics expression mentioned in Sec. III; finally, we investigate whether the regular form is stable if the rear plate is stimulated by an external horizontal loading within a certain range.

A. Emergent dynamics and configurations in a two-plate self-propelled system

For two self-propelled plates with identical flapping amplitude ($A_1 = A_2$) and frequency in tandem, the emergent stable configurations with quantized gap spacings in the in-phase scenario have been noticed.[6,20] Here, two plates with different flapping amplitudes and flapping phase would be further discussed based on the analysis of vortex–body interaction.

Here, first we would like to see the results of the in-phase flapping cases. The evolutions of gap spacing G for in-phase cases with different A_2 are shown in Fig. 6(a). In all simulations, the flapping amplitude of the front plate is fixed as $A_1 = 0.5$. It is seen that for the case with A_2

$= A_1$, G keeps constant first ($t < 2.5$), then it decreases, and eventually, two plates reach a stable state with an equilibrium G, which is referred to as G^{eq}. The procedure can be understood as follows. Initially, the cruising speeds of the two plates are identical before the follower encounters the vortices shed from the leader. After it encounters the vortices, then the follower would accelerate and eventually due to the vortex–body interaction, G would be passively adjusted to G^{eq}. In the equilibrium state, the two plates cruise with an identical cruising speed and $G \approx \lambda$, where λ ($= |\int_0^T u_1(t)dt| = 5.5263$) is the streamwise spatial period of the reversed Kármán vortex street generated by the front plate. Actually, not only $G^{eq} \approx \lambda$ but also $G^{eq} \approx 2\lambda, 3\lambda\ldots\ldots$ are equilibrium locations if the initial G is close to those G^{eq}.

For the other cases with different A_2, if the follower's flapping amplitude $A_2 > A_1$, e.g., $A_2 \in [0.5, 0.65]$, the situation looks similar to that of $A_1 = A_2 = 0.5$, i.e., G decreases initially and then adjust to a constant. However, if A_2 is too large, e.g., $A_2 = 0.7$, the follower makes much effort to flap than the leader because generally speaking, a larger flapping amplitude means more energy input. In this way, G continuously decreases and the follower may collide with the leader. On the other hand, if A_2 is smaller than 0.5, e.g., $A_2 = 0.4$, the stable configuration may still emerge. However, in the case, because the follower makes less effort, G increases initially and it has a risk of falling behind. If A_2 is further smaller, e.g., $A_2 = 0.35$, G would gradually become large enough so that two plates cruise independently with different speed. There is no stable configuration. It is also noticed that for all of the above cases with stable configuration, the equilibrium gap spacing $G^{eq}(= \int_t^{t+T} G/Tdt)$ decreases as A_2 increases [see Fig. 6(a)].

For all of the cases having a stable configuration, the rear plate would be trapped through different vortex–body interaction. The interaction is characterized by superimposing the leading-edge trajectories of the rear plates on the vortex street generated by the front plate. The corresponding trajectories are shown in Fig. 6(b). According to Zhu et al.,[6] the trajectories of the rear plate would be locked onto the vortex centers. However, "locking onto the vortex centers" is not so accurate. Strictly speaking, locking onto the vortex centers means that the head of the plate passes through the centers of the
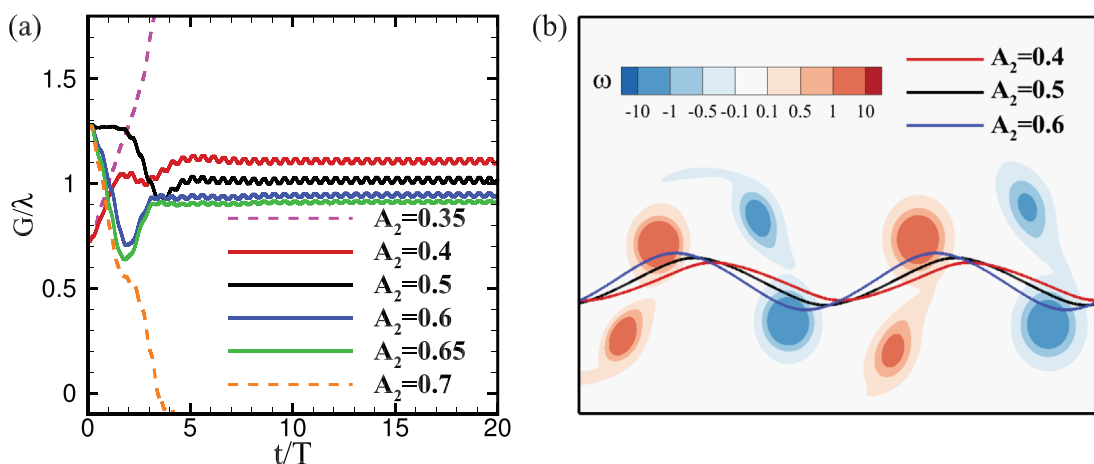

FIG. 6. (a) Gap spacing as a function of time for in-phase scenario ($\Delta\phi = 0$). In all cases $A_1 = 0.5$, while A_2 ranges from 0.35 to 0.7. λ ($= \int_{t'}^{t'+T} u_1(t)dt = 5.5263$) is the streamwise spatial period of the reversed Kármán vortex street generated by the front plate. (b) Superimposition of the leading-edge trajectories of the rear plates with $A_2 = 0.4, 0.5,$ and 0.6 on the vortex street.

shedding vortices ahead of it at its maximum/minimal lateral locations ($y_2 = \pm A_2$, $\dot{y}_2 = 0$). It is seen from Fig. 6(b) that in all cases including the case of $A_2 = 0.5$, the trajectory of the rear plate does not pass through the vortex core exactly. Actually, as far as we know, besides the "vortex locking" mode, "slaloming between the vortex cores" also has been found as an alternative vortex–body interaction for passive oscillations of two tandem flexible filaments.[8] Slaloming between the vortex cores means that the head of the rear plate passes through the middle points between each pair of vortices ahead of it. Here, we found that for the stable self-propulsive tandem configurations, the trajectories of the rear plate may be neither slaloms between nor is locked onto the vortex cores, and the state between these two modes may be more common.

From Fig. 6(b), we can see that the trajectory in the case of $A_2 = 0.6$ is close to, but not exactly, the "locking" mode. The trajectory in the case of $A_2 = 0.4$ is close to the "slaloming" mode. In the above two cases, at equilibrium states, both cruising speeds are identical to that of an isolated plate flapping with $A = 0.5$. To explain it, the effective flapping velocity of the rear plate v_e is introduced. It means the relative vertical velocity of the leading edge of the rear plate with respect to the local vertical velocity induced by the reversed Kármán vortex street. According to the reduced-order model (ROM),[31,34] the time-averaged thrust on the rear plate ($\bar{T}_2$) is proportional to the square of its effective flapping velocity v_e, and the time-averaged drag ($\bar{D}_2$) depends on the square of the rear plate's cruising speed. Since, at equilibrium states, the cruising speed is fixed, the time-averaged drag on the rear plate ($\bar{D}_2$) can also be approximated as fixed. Therefore, at equilibrium states, even when the flapping amplitude of the rear plate (v_2) changes, the time-averaged thrust ($\bar{T}_2$) is unchanged, and its effective flapping velocity v_e is similar to the flapping velocity (v_1) of the front plate with $A = 0.5$. For an isolated plate with $A = 0.6$, its cruising speed should be larger than that of the isolated case $A = 0.5$. The locking interaction mode in the cases of $A_2 = 0.6$ inhibits the full-speed cruising of the rear plate. The inhibition is due to the smaller v_e compared to that of an isolated plate. In this way, less vorticity and less thrust are generated on the plate, which inhibits the full-speed

cruising. For the slaloming interaction mode in the case of $A_2 = 0.4$, the situation is reversed. More details can be found in Sec. IV B.

To identify the effect of phase difference $\Delta\phi$ on stable configurations, as shown in Fig. 7(a), we explored the parameter space of stable configurations with different combinations of flapping amplitude A_2 and phase difference $\Delta\phi$. It is seen that whether or not stable configurations can be formed is independent of the phase difference. For clarity, cases of $A_1 = A_2 = 0.5$ but $\Delta\phi \neq 0$ are discussed. For all phase difference, stable configurations emerge spontaneously. Figure 7(b) shows the equilibrium gap spacing G^{eq}/λ as a function of $\Delta\phi$. It is seen that for each G_0, G^{eq} is a piecewise linear function of $\Delta\phi$. It is also seen that for each G_0, at a certain $\Delta\phi$ there is a jump of G^{eq}. The jump of G^{eq} is the streamwise spatial period of the reversed Kármán vortex street generated by the front plate, λ. Because of the spatial periodicity of the vortex street, for a specific G_0, there is a unstable critical phase lag $\Delta\phi_c$. If $\Delta\phi < \Delta\phi_c$, the rear plate eventually converges to the relative rearward equilibrium position, and vice versa.

Although in all cases G^{eq} may be different, we found that in all cases, the trajectories of the head of the rear plate with respect to the shedding vortices are all identical to the in-phase case, i.e., $\Delta\phi = 0$ [the black solid line in Fig. 6(b)]. It seems that the rear plate can adjust G^{eq} to match the specific vortex–body interaction. In other words, the phase difference does not affect the vortex–body interaction.

B. Force on the rear plate in terms of local vortical structures

In all of the above freely self-propelled cases, at the equilibrium states, the time-averaged hydrodynamic forces on the rear plate are zero. However, we want to investigate how different vortex–body interactions lead to nonzero hydrodynamic force. To figure out the connection, we created an arbitrary vortex–body interaction in the following way. For convenience, the simulations were performed in an inertial coordinate system moving with velocity U_e in the negative x-direction, where U_e is the equilibrium cruising speed of the self-propulsive case that we obtained in advance. In the inertial frame, the
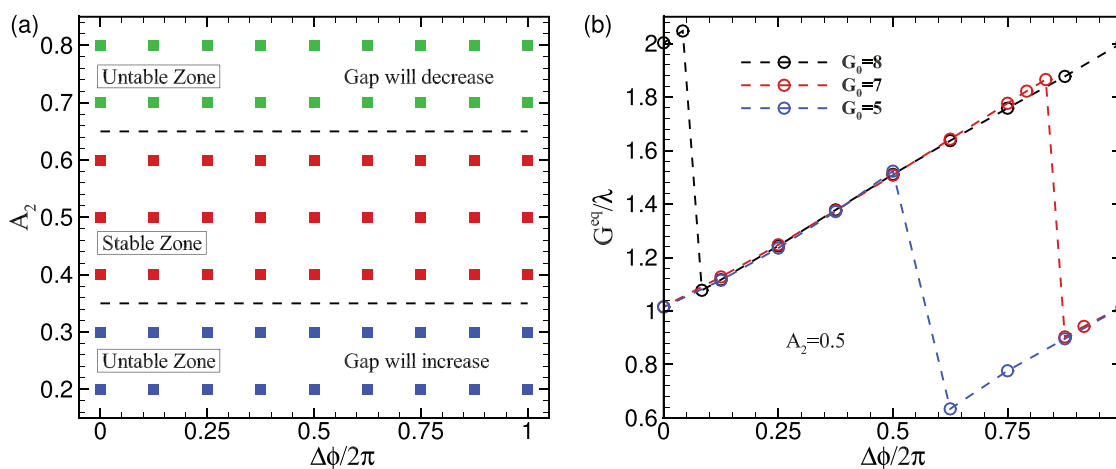

FIG. 7. (a) Parameter space $(\Delta\phi, A_2)$ for the stability of orderly configurations of two independently flapping plates with $A_1 = 0.5$. (b) Equilibrium gap spacing G^{eq}/λ as a function of phase difference $\Delta\phi$ for three different initial gap spacing G_0. In all cases $A_1 = A_2 = 0.5$. Each point denotes a case.

oncoming flow has a uniform longitudinal velocity of U_e and the longitudinal locations of the plates are fixed. From about discussion, we know that in self-propulsive cases with different $\Delta\phi$, the rear plate would automatically adjust the gap spacing to achieve the identical vortex–plate interaction. Hence, all kinds of vortex–plate interactions may be achieved through fixing the gap spacing G_a but adopting different $\Delta\phi$ or alternatively, fixing $\Delta\phi$, e.g., $\Delta\phi = 0$ but adopting different G_a. Since the two ways to achieve the different vortex–plate interaction are analogous, in the following discussion we adopted the latter way ($\Delta\phi = 0$ is fixed but G_a is changed).

Figure 8(a) shows the time-averaged horizontal force $\bar{F}_x (= \int_t^{t+T} F_x(t)dt/T)$ on the rear plate as a function of G_a for the in-phase scenarios ($\Delta\phi = 0$). It is seen that $\bar{F}_x$ changes approximately periodically with G_a, with a period of λ. There are several discrete points with $\bar{F}_x = 0$, such as $G_a = 1.03\lambda, 1.50\lambda, 2.03\lambda, \ldots$. Only the gap spacings with negative $d\bar{F}_x/dG_a$, i.e., $G_a = 1.03\lambda, 2.03\lambda, \ldots$, correspond to the G_as of the self-propulsive stable configurations. The net horizontal force near the G_as is a springlike restoring force as discussed by Ramananarivo et al.[13] and Peng et al.[20]

As is implied by Figs. 6 and 8(a), the shedding vortices can play either a destructive or constructive role in different vortex–body interactions. To identify the possible formation of vorticity field of different interactions, we calculated the strength of vorticity generated by the rear plate in a period. The strength of newly generated vorticity on the rear plate is obtained by subtracting the strength of the closest upstream vortex pair from the strength of the closest downstream vortex pair. It is noticed that in the $2P$ wake shed by the front plate, the strengths of the stronger vortex (≈ 2) and weaker vortex (≈ 1) are of the same order of magnitude as that of the newly generated vorticity from the rear plate. From Fig. 8(a), we can see that the strength of newly generated vorticity on the rear plate is inversely related to $\bar{F}_x$. According to the reduced-order model,[31,34] we can get a simple understanding that the time-averaged drag ($\bar{D}_2$) on the rear plate almost does not change with G_a. Combing $\bar{F}_x = -\bar{T}_2 + \bar{D}_2$, we can conclude a simple relationship between the hydrodynamic thrust and vorticity generation on the rear plate: if the vorticity generation on the rear plate is suppressed, the thrust effect on it is weakened; if the vorticity generation on the rear plate increases, the thrust effect will be enhanced. In addition, using the simplified model,[34] we can obtain

the reduced-order relationship between the time-averaged hydrodynamic force $\bar{F}_x$ and the gap spacing G_a, i.e.,

$$\bar{F}_x = c_t \cos\left(2\pi\frac{G_a + 1}{\lambda}\right) - \frac{c_t}{2}, \tag{16}$$

where c_t is the thrust coefficient and selected as 0.8.[34] Figure 8(b) compares the time-averaged hydrodynamic force $\bar{F}_x$ calculated by the reduced-order model [Eq. (16)] with the present result. It is seen that the simplified model can only predict the trend of horizontal force $\bar{F}_x$ with gap spacing G_a, but not the exact magnitude of the force.

Here, we choose three typical gap spacings, $G_a = 0.81\lambda, 1.03\lambda$, and 1.27λ, to clarify how the vortex–plate interaction influences the force on the rear plate. As can be seen from Fig. 9(a), $G_a = 0.81\lambda, 1.03\lambda$, and 1.27λ correspond to the maximum, zero, and minimum $\bar{F}_x$, respectively. To analyze the vortex–body interaction, in Fig. 9(a), the trajectories of the leading edge of the rear plate are superimposed on the vortex street generated by the isolated front plate. The instantaneous vorticity fields for the three cases at $t/T = 0$ are shown in Figs. 9(b)–9(d) (Multimedia view). We can see that in the case of $G_a = 0.81\lambda$ [see Fig. 9(b)], the rear plate passes through the cores of the stronger vortices within each vortex pair. It suppresses the deformation of the plate (figure is not shown) and further suppresses the generation and separation of vorticity on the rear plate. The new shed vortex by the rear plate will be entangled with the environmental vorticity of the same sign. For the case of $G_a = 1.27\lambda$ [see Fig. 9(d)], the rear plate slaloms between the vortex cores, which enhances the deformation of the plate, and further enhances the generation and separation of vorticity on the rear plate. The new shed vortex by the rear plate will be entangled with the environmental vorticity of the inverse sign. For the case of $G_a = 1.03\lambda$ [see Fig. 9(c)], the rear plate passes through a small portion of the environmental vortex, which makes the deformation of the rear plate similar to that of the front plate.

To quantitatively investigate the relationship between the force on the rear plate and the local flow structures around it, the force formula [Eq. (15)] is used to calculate the force. The domain V in the formula is chosen to contain the nearby environmental vortices and the vortices connecting with the rear plate [see Fig. 10(c)]. In the three cases, the forces on the rear plate have been well predicted and they are consistent with the direct integral of Lagrangian force F_s on the plate (figure is not shown). Our previous investigation[48] has also
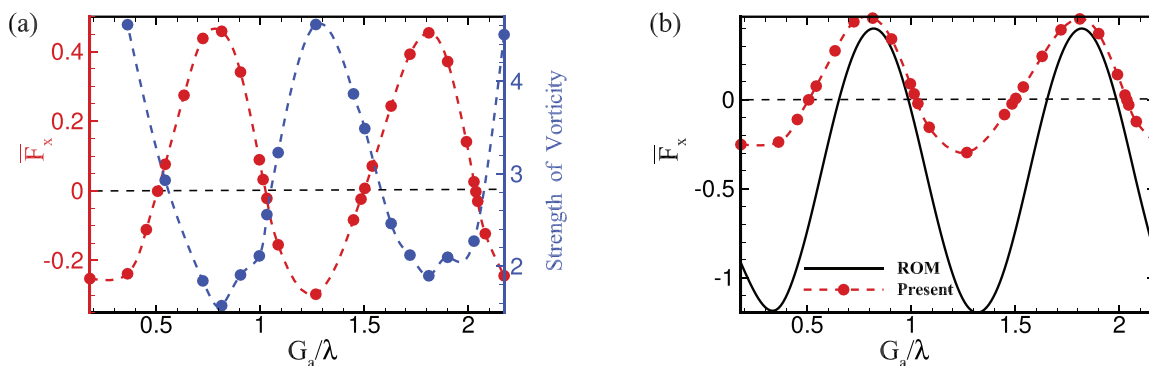

FIG. 8. (a) The time-averaged x-component force $\bar{F}_x$ and the strength of the newly generated vorticity on the rear plate in a cycle vs the fixed gap spacing G_a/λ for in-phase flapping. (b) Comparison of time-averaged hydrodynamic force $\bar{F}_x$ calculated by the reduced-order model (ROM) [Eq. (16)] with the present numerical results.
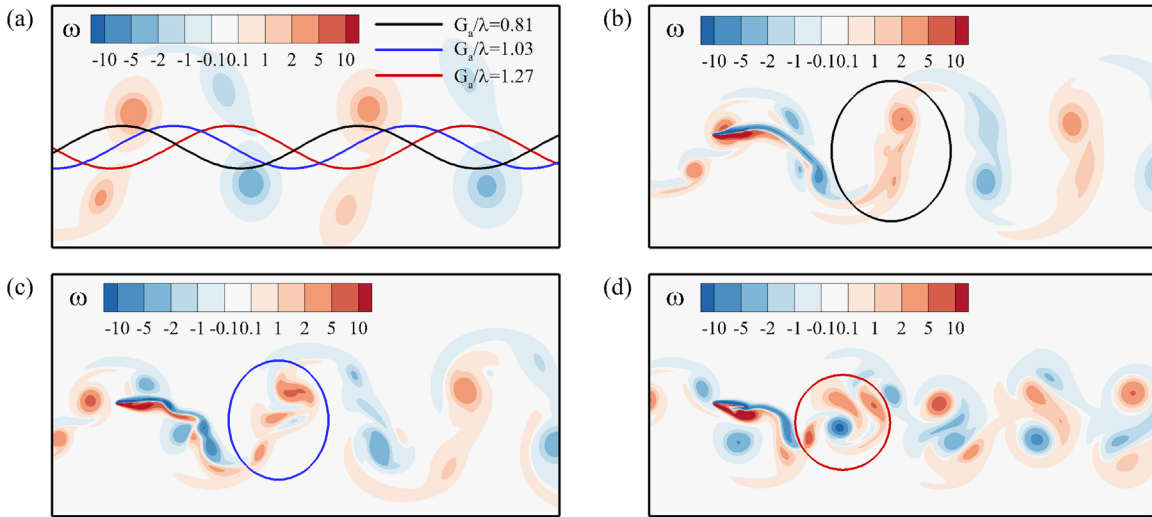
FIG. 9. (a) Superimposition of the leading-edge trajectories of the rear plates on the vortex street generated by the front plate for $G_a/\lambda = 0.81$ (black solid line), $G_a/\lambda = 1.03$ (blue solid line) and $G_a/\lambda = 1.27$ (red solid line). The instantaneous vorticity fields of the three cases at $t/T = 0$ are shown in (b), (c), and (d), respectively. Multimedia views: https://doi.org/10.1063/5.0079818.1; https://doi.org/10.1063/5.0079818.2; https://doi.org/10.1063/5.0079818.3

provided evidence for the reliability of Eq. (15). The horizontal forces F_x contributed by the moment of the vorticity derivative $\boldsymbol{F}_{MVD}(= -\int_V \boldsymbol{x} \times \frac{d(\rho\boldsymbol{\omega})}{dt} dV)$ for the three cases are shown in Fig. 10(a). The standard results are calculated by the direct integral of Lagrangian force $\boldsymbol{F}_s$ on the plate. It is seen that the x-component of $\boldsymbol{F}_{MVD}$ is close to that of the standard results. Therefore, the hydrodynamic force is

mainly contributed by $\boldsymbol{F}_{MVD}$. The contribution from the surface integral term on Σ is minor. Hence, the force is strongly dominated by the vortical structures close to the rear plate.

The contribution of the reversed Kármán vortices is also calculated. Its direct contribution is negligible. Taking the case of $G_a = 1.27\lambda$ as an example [see Fig. 10(b)], we found that the forces contributed by
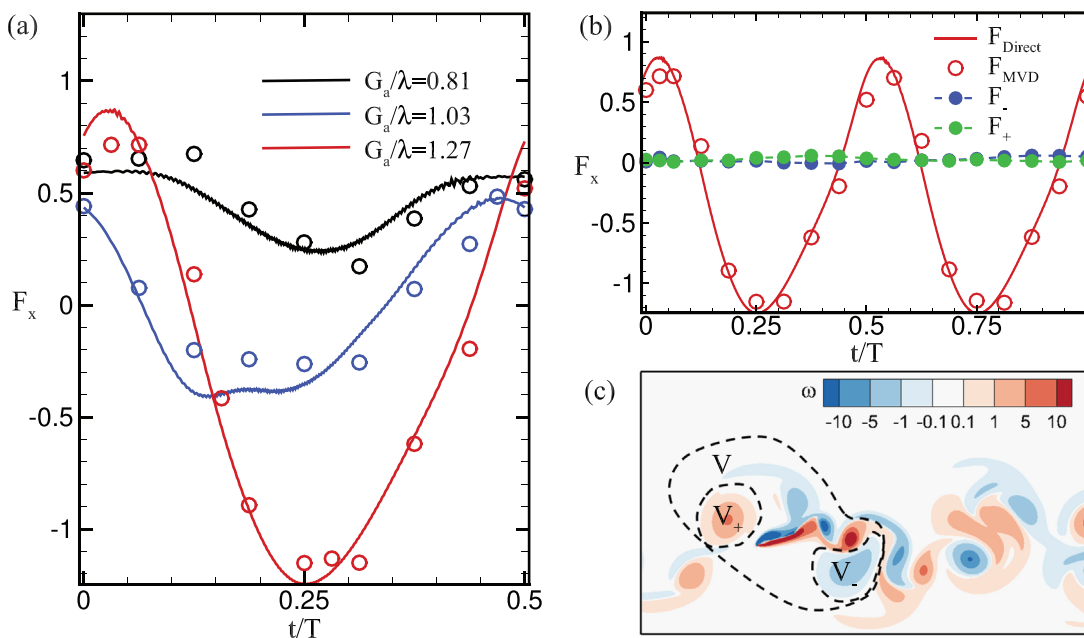

FIG. 10. (a) The evolution of horizontal hydrodynamic force calculated directly by the integral of Lagrangian force $\boldsymbol{F}_s$ on the plate (solid lines) and that contributed by $\boldsymbol{F}_{MVD} = -\int_V \boldsymbol{x} \times \frac{d(\rho\boldsymbol{\omega})}{dt} dV$ (circles) for the three cases. (b) The evolution of F_x for the case of $G_a = 1.27\lambda$, where F_- and F_+ are integrated on domains V_- and V_+ [as shown in (c)], respectively. (c) The instantaneous vorticity distribution at $t/T = 1/4$ for the case of $G_a = 1.27\lambda$.

the positive and negative stronger vortices (F_+ and F_-), whose domains are denoted by V_+ and V_- in Fig. 10(c), are almost zero over the entire period. It indicates that the influence of the reversed Kármán vortices on the force of the rear plate is not by its direct contribution (F_+ and F_- can be ignored), but in some indirect way.

Next, we will explain how the reversed Kármán vortex indirectly affects the generation of vorticity on the rear plate and thus affects the hydrodynamic force. When the rear plate encounters the oncoming flow induced by the reversed Kármán vortex street, there is an effective vertical flapping velocity of the rear plate v_e. Variations of v_e in a period for the three cases are shown in Fig. 11(a). For the case of $G_a = 0.81\lambda$, v_e magnitude is essentially small, which leads to less vorticity generation during a period. For the case of $G_a = 1.27\lambda$, a larger magnitude of v_e of the rear plate would generate stronger vortices close to the leading edge. For the case of $G_a = 1.03\lambda$, the curve of v_e of the rear plate almost have the same magnitude as that of the front one, but with a phase shift. The strength of the new vorticity generated on the rear plate approximately has the magnitude as that of the reversed Kármán vortices shed by the front one. The distributions of $d\omega/dt$ on the rear plate at two typical moments t_1 and t_2, when instantaneous minimum and maximal horizontal forces, i.e., F_{xMIN} and F_{xMAX} are generated, respectively, are shown in Fig. 11(b). It is seen that the vorticity is mainly generated around the leading edge. At $t = t_1$, there is negative vorticity generated on the leading edge, and the case of $G_a = 1.03\lambda$ generates the strongest negative vorticity near the leading edge among all of the three cases.

To quantitatively relate the force on the rear plate to the generation and evolution of vorticity on it, the domain V of the force formula Eq. (15) is contracted to the body force domain V_{bf}. The force on the plate can be expressed as

$$F = F_{G\&BVF} + F_F, \tag{17}$$

$$F_{G\&BVF} = -\int_{V_{bf}} x \times \frac{d(\rho\omega)}{dt}dV + \int_{\partial V_{bf}} \mu x \times (n \cdot \nabla\omega)dS, \tag{18}$$

$$F_F = \int_{\partial V_{bf}} \mu\omega \times n dS, \tag{19}$$

where $F_{G\&BVF}$ is contributed by the generation of vorticity $d(\rho\omega)/dt$ and viscous force resulting from the boundary vorticity flux ($n \cdot \nabla\omega$), and F_F can be regarded as the friction effect. Figure 12(a) shows that Eq. (17) can predict the force well. The green points and lines in Fig. 12 correspond to the forces on the front plate. As shown in Fig. 12(b), for different vortex–plate interaction, the horizontal force contributed by the friction term Eq. (19) keeps positive with little variation over time. The difference of $F_F \cdot e_x$ between different cases is little. The result is consistent with the prediction of reduced-order model, which shows that the drag on the rear plate D_2 is similar to that of the front plate D_1. The variation of F is mainly contributed by the counterbalance and synergy between vorticity generation and boundary vorticity flux on the plate, i.e., $F_{G\&BVF}$. In a reduced order sense, the thrust on the plate can be approximately $-F_{G\&BVF} \cdot e_x$. It is also seen from Figs. 12(b) and 9 that the thrust effects are enhanced for slaloming interaction mode and are weakened for locking interaction mode.

The generation of vorticity mainly happens at the leading edge of the rear plate as shown in Fig. 11(b). Figure 13(a) shows that the boundary vorticity flux $n \cdot \nabla\omega$ mainly happens near the leading edge of the rear plate at $t = t_1$. It is seen that, with the increase in G_a, the boundary vorticity flux on the upper surface of the rear plate changes more dramatically, because of more flow separations occurring on the upper surface [see Figs. 9(b)–9(d)]. Figure 13(b) shows that the boundary vorticity flux also mainly happens near the leading edge at $t = t_2$, except there is a significant boundary vorticity flux at the trailing edge in the case of $G_a = 1.27\lambda$. This instance $t = t_2$ usually corresponds to the moment with a flapping speed of almost zero, when the inertia of flow plays a major role.

C. Stable configuration of the rear plate with an external horizontal loading

To investigate whether the stable configurations would emerge if the rear plate is stimulated by an external horizontal loading, we simulate the self-propulsion of two flapping plates with identical flapping motions swimming in tandem. Here, in all cases, different external
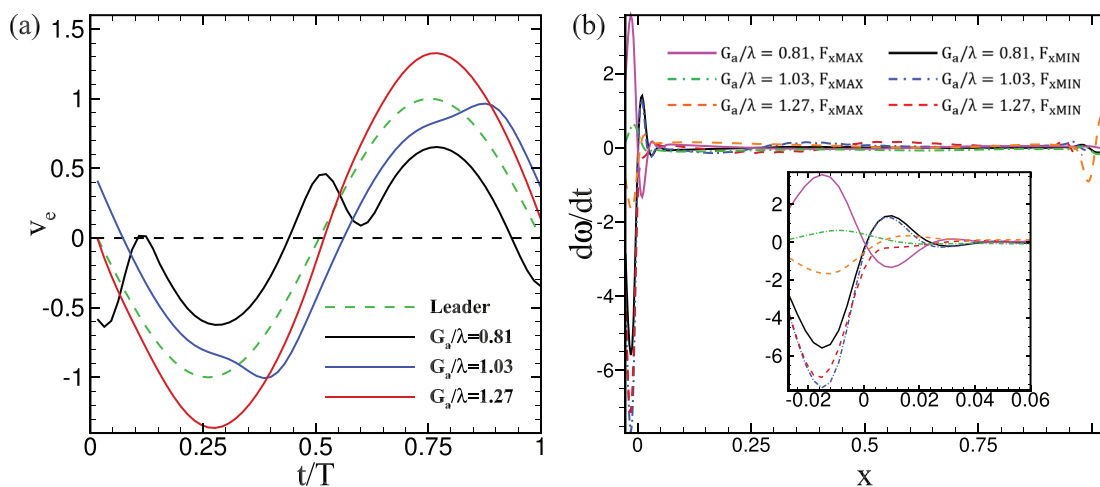

FIG. 11. (a) The evolution of the effective vertical flapping velocity of the rear plate v_e. (b) The distribution of $d\omega/dt$ along the plate at instances when maximal and minimum horizontal forces, i.e., F_{xMAX} and F_{xMIN}, occur.
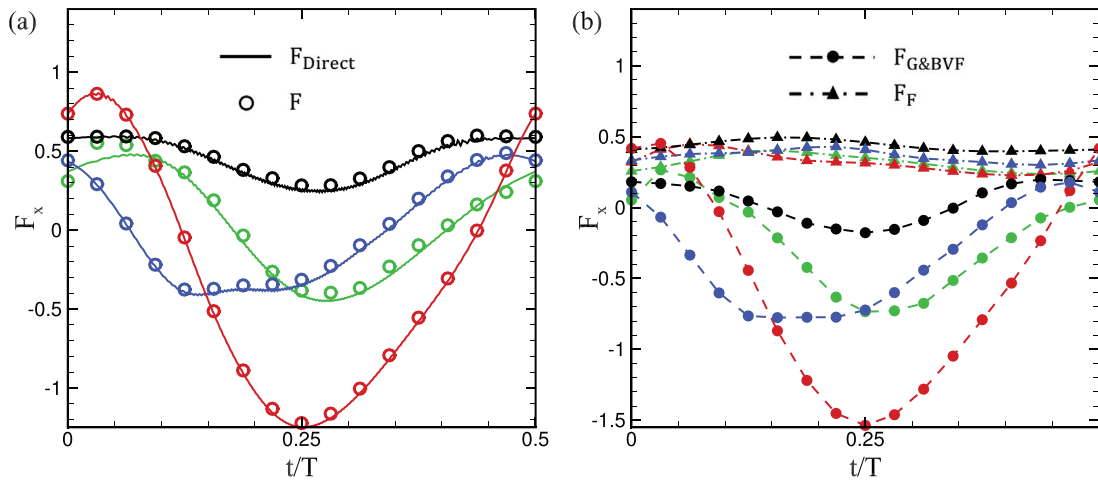
FIG. 12. The evolution of the hydrodynamic force on the plate in half a cycle. The forces on the rear plates with $G_a/\lambda = 0.81, 1.03, 1.27$ and on the front plate are denoted by color black, blue, red and green, respectively. (a) The forces calculated by Eq. (17) (circles) and the integral of the Lagrangian force F_s (solid lines). (b) The evolution of force components $F_{G\&BVF}$ and F_F, calculated by Eqs. (18) and (19), respectively.

horizontal loadings F_{xE} are applied to the leading edge of the rear plate. The result is shown in Fig. 14(a). It is seen that when $F_{xE} \in [-0.3, 0.3]$, the equilibrium states still emerge and in each equilibrium state, the rear plate is trapped in the orderly configuration. In addition, G^{eq} changes linearly with F_{xE}. It is noticed that when $|F_{xE}|$ is large enough, e.g., out of the range $[-0.3, 0.3]$, no stable configuration would be formed and terminally the two plate cruise independently.

The trajectories of the rear plates superimposing on the vortex street in the cases of $F_{xE} = -0.3$, 0, and 0.3 are shown in Fig. 14(b). They represent different vortex–body interactions. For the case of $F_{xE} = 0.3$, the vortex–body interaction mode is the slaloming mode. The rear plate would obtain an enhanced thrust to balance the external loading. For the case of $F_{xE} = -0.3$, the plate would obtain a

weakened thrust by a mode close to the locking mode. Hence, to balance the external force, a reversed hydrodynamic force is achieved through a specific mode of vortex–plate interaction.

V. CONCLUDING REMARKS

We studied the hydrodynamic force induced by vortex–body interactions in orderly formations of two flapping flexible plates in a tandem configuration in a two-dimensional incompressible viscous fluid. We simulated two types of settings for the two-plate self-propelled system: (i) two plates with independent flapping amplitude, A_i; (ii) two plates with identical flapping amplitude, and an external horizontal loading F_{xE} is exerted on the rear plate. It is found that, whether the rear plate changes its flapping amplitude or is exerted an
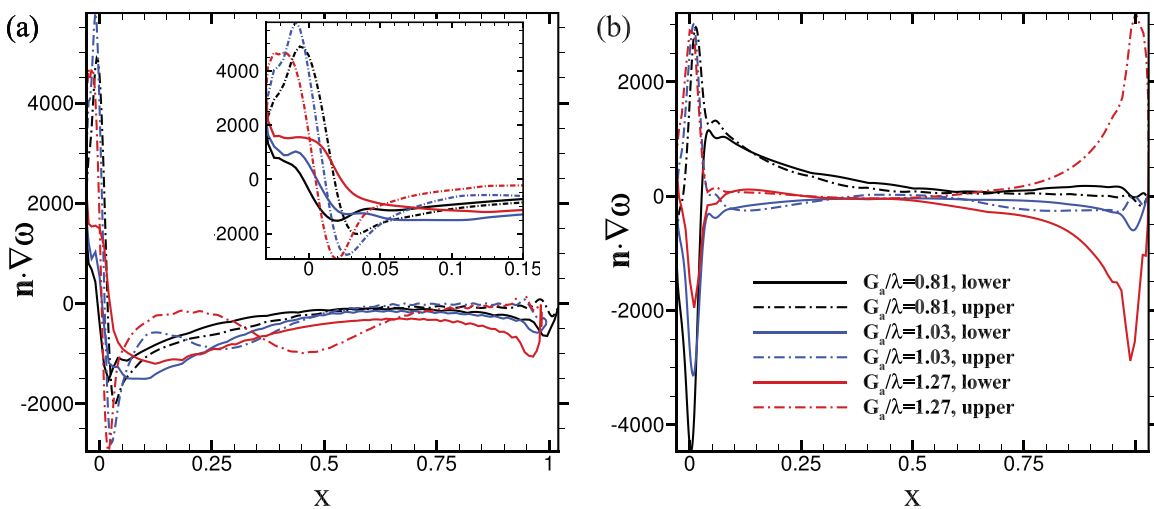

FIG. 13. The distribution of boundary vorticity flux $\mathbf{n} \cdot \nabla \omega$ on ∂V_{bf} at the instances with (a) minimum horizontal force F_{xMIN} ($t = t_1$) and (b) maximal horizontal force F_{xMAX} ($t = t_2$) during the downward flapping process. The inset in (a) is a local zoom-in view.
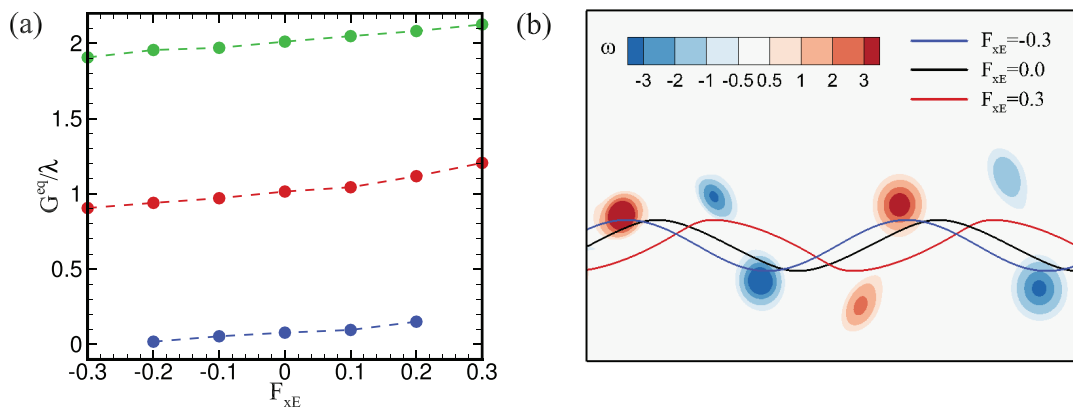
FIG. 14. (a) Gap spacing G^{eq}/λ as a function of the constant external loading F_{xE} on the rear plate. (b) Vortex–body interaction in three cases with different F_{xE}.

external horizontal loading, the vortex street shed by the front plate has a certain ability to trap the rear plate into the orderly configuration. In other words, at each equilibrium state, the rear plate may be trapped into a specific vortex–plate interaction mode and maintain the same propulsion velocity as the front plate. Vortex–body interaction is generally characterized by the trajectory of the rear plate with respect to the oncoming reversed Kármán vortex street. From simulations of case (i), we found that the stability of orderly configurations and the vortex–plate interaction are not affected by phase difference $\Delta\phi$.

To clarify the origin of the hydrodynamic force on the rear plate in different vortex–plate interaction, vorticity-based representation and interpretation are proposed. We found the hydrodynamic force on the flapping plate is strongly dominated by the vortical structures close to the flapping plate, and more specifically, it is directly related to the vorticity generation on the plate as well as viscous forces resulting from its subsequent evolution.

To our knowledge, it is the first time to use vorticity-based representation instead of the simplified analytical model to quantitatively explain the physical process of the influence of vortex–plate interaction on the hydrodynamic force of collective motion. Actually, the reversed Kármán vortices would indirectly affect the hydrodynamic force exerted on the rear plate by modulating the generation and distribution of vorticity on it. When the rear plate is slaloming between vortex cores or close to the state, the vertical momentum of the vortices shedding from the front plate can be successfully harvested. Under the circumstances, the vorticity generation and the thrust effect are enhanced. Therefore, the rear plate can reduce its flapping amplitude. In this way, the hydrodynamic advantage is achieved by the rear plate. On the other hand, the vortex locking behavior of the rear plate is not favorable, because the vorticity generation and the thrust effect are suppressed. There is no hydrodynamic advantage for the rear plate.

Finally, it should be pointed out that although the geometric shape and the actuation of our model are simplified, the current work is still essential for understanding the collective behaviors in macroscopic swimmers. It also inspires some constructive applications. For example, the follower can exploit more surrounding vortical momentum by appropriately reducing its flapping amplitude while maintaining the stable configuration.

AUTHOR DECLARATIONS
Conflict of Interest

The authors have no conflicts to disclose.

DATA AVAILABILITY

The data that support the findings of this study are available from the corresponding author upon reasonable request.

APPENDIX A: DERIVATIVE MOMENTUM TRANSFORMATION

A vectorial integral identity, named *derivative-moment-transformation*, is used in developing the theory: in n-dimensional space with $n = 2, 3$, set $k = n - 1$, for any piecewise differentiable vector field $\boldsymbol{g}$, there is

$$\int_V \boldsymbol{g} dV = \frac{1}{k}\int_V \boldsymbol{x} \times (\nabla \times \boldsymbol{g}) dV - \frac{1}{k}\int_{\partial V} \boldsymbol{x} \times (\boldsymbol{n} \times \boldsymbol{g}) dS, \quad (A1)$$

where $\boldsymbol{x}$ is the position vector and ∂V is the boundary of domain V. Note that the equation is independent of the origin of position vector.

REFERENCES

[1] D. H. Cushing and F. R. H. Jones, "Why do fish school?," Nature **218**, 918–920 (1968).

[2] D. Weihs, "Hydromechanics of fish schooling," Nature **241**, 290–291 (1973).

[3] F. E. Fish, "Energetics of swimming and flying in formation," Comments Theor. Biol. **5**, 283–304 (1999).

[4] C. K. Hemelrijk and H. Hildenbrandt, "Schools of fish and flocks of birds: Their shape and internal structure by self-organization," Interface Focus **2**, 726–737 (2012).

[5] L. Li, M. Nagy, J. M. Graving, B. C. Joseph, G. M. Xie, and I. D. Couzin, "Vortex phase matching as a strategy for schooling in robots and in fish," Nat. Commun. **11**, 5408 (2020).

[6] X. J. Zhu, G. W. He, and X. Zhang, "Flow-mediated interactions between two self-propelled flapping filaments in tandem configuration," Phys. Rev. Lett. **113**, 238105 (2014).

[7] J. C. Liao, "A review of fish swimming mechanics and behaviour in altered flows," Philos. Trans. R. Soc., B **362**, 1973–1993 (2007).

[8] L. B. Jia and X. Z. Yin, "Passive oscillations of two tandem flexible filaments in a flowing soap film," Phys. Rev. Lett. **100**, 228104 (2008).

[9] I. L. Bajec and F. H. Heppner, "Organized flight in birds," Anim. Behav. **78**, 777–789 (2009).

[10] S. J. Portogal, T. Y. Hubel, J. Fritz, S. Heese, D. Trobe, B. Voelkl, S. Hailes, A. M. Wilson, and J. R. Usherwood, "Upwash exploitation and downwash avoidance by flap phasing in ibis formation flight," Nature **505**, 399–402 (2014).

[11] M. Daghooghi and I. Borazjani, "The hydrodynamic advantages of synchronized swimming in a rectangular pattern," Bioinspiration Biomimetics **10**, 056018 (2015).

[12] C. K. Hemelrijk, D. A. P. Reid, H. Hildenbrandt, and J. T. Padding, "The increased efficiency of fish swimming in a school," Fish Fish. **16**, 511–521 (2015).

[13] S. Ramananarivo, F. Fang, A. Oza, J. Zhang, and L. Ristroph, "Flow interactions lead to orderly formations of flapping wings in forward flight," Phys. Rev. Fluids **1**, 071201 (2016).

[14] S. G. Park and H. J. Sung, "Vortex interaction between two tandem flexible propulsors with a paddling-based locomotion," J. Fluid Mech. **793**, 612–632 (2016).

[15] A. Gao and M. S. Triantafyllou, "Independent caudal fin actuation enables high energy extraction and control in two-dimensional fish-like group swimming," J. Fluid Mech. **850**, 304–335 (2018).

[16] S. Verma, G. Novati, and P. Koumoutsakos, "Efficient collective swimming by harnessing vortices through deep reinforcement learning," Proc. Natl. Acad. Sci. U. S. A. **115**, 5849–5854 (2018).

[17] S. G. Park and H. J. Sung, "Hydrodynamics of flexible fins propelled in tandem, diagonal, triangular and diamond configurations," J. Fluid Mech. **840**, 154–189 (2018).

[18] M. J. Lighthill, *Mathematical Biofluiddynamics* (SIAM, Philadelphia, 1975).

[19] Z.-R. Peng, H. B. Huang, and X.-Y. Lu, "Collective locomotion of two closely spaced self-propelled flapping plates," J. Fluid Mech. **849**, 1068–1095 (2018).

[20] Z.-R. Peng, H. B. Huang, and X.-Y. Lu, "Hydrodynamic schooling of multiple self-propelled flapping plates," J. Fluid Mech. **853**, 587–600 (2018).

[21] L. Ristroph and J. Zhang, "Anomalous hydrodynamic drafting of interacting flapping flags," Phys. Rev. Lett. **101**, 194502 (2008).

[22] S. Alben, "Wake-mediated synchronization and drafting in coupled flags," J. Fluid Mech. **641**, 489–496 (2009).

[23] S. Kim, W.-X. Huang, and H. J. Sung, "Constructive and destructive interaction modes between two tandem flexible filaments in a uniform flow," J. Fluid Mech. **661**, 511–521 (2010).

[24] G. V. Lauder, E. J. Anderson, J. Tangorra, and P. G. A. Madden, "Fish biorobotics: Kinematics and hydrodynamics of self-propulsion," J. Exp. Biol. **210**, 67–80 (2007).

[25] D. Rival, D. Schonweitz, and C. Tropea, "Vortex interaction of tandem pitching and plunging plates: A two-dimensional model of hovering dragonfly-like flight," Bioinspiration Biomimetics **6**, 016008 (2011).

[26] B. M. Boschitsch, P. A. Dewey, and A. J. Smits, "Propulsive performance of unsteady tandem hydrofoils in an in-line configuration," Phys. Fluids **26**, 051901 (2014).

[27] E. Uddin, W.-X. Huang, and H. Sung, "Actively flapping tandem flexible flags in a viscous flow," J. Fluid Mech. **780**, 120–142 (2015).

[28] J. Warkentin and J. Delaurier, "Experimental aerodynamic study of tandem flapping membrane wings," J. Aircr. **44**, 1653–1661 (2007).

[29] T. M. Broering and Y.-S. Lian, "The effect of phase angle and wing spacing on tandem flapping wings," Acta Mech. Sin. **28**, 1557–1571 (2012).

[30] A. D. Becker, H. Masoud, J. W. Newbolt, M. Shelley, and L. Ristroph, "Hydrodynamic schooling of flapping swimmers," Nat. Commun. **6**, 8514 (2015).

[31] J. W. Newbolt, J. Zhang, and L. Ristroph, "Flow interactions between uncoordinated flapping swimmers give rise to group cohesion," Proc. Natl. Acad. Sci. U. S. A. **116**, 2419–2424 (2019).

[32] X. Lin, J. Wu, T. Zhang, and L. Yang, "Phase difference effect on collective locomotion of two tandem autopropelled flapping foils," Phys. Rev. Fluids **4**, 054101 (2019).

[33] J. Ryu, J. M. Yang, S. G. Park, and H. J. Sung, "Phase-mediated locomotion of two self propelled flexible plates in a tandem arrangement," Phys. Fluids **32**, 041901 (2020).

[34] L. L. Kang, Z. R. Peng, H. B. Huang, X.-Y. Lu, and W. C. Cui, "Active external control effect on the collective locomotion of two tandem self-propelled flapping plates," Phys. Fluids **33**, 101901 (2021).

[35] T. Y. Wu, "Swimming of a waving plate," J. Fluid Mech. **10**, 321–344 (1961).

[36] T. Y. Wu and A. T. Chwang, "Extraction of flow energy by fish and birds in a wavy stream," in *Swimming and Flying in Nature* (Springer, 1975).

[37] T. von Kármán and W. R. Sears, "Airfoil theory for non-uniform motion," J. Aeronaut. Sci. **5**, 379–390 (1938).

[38] W. R. Sears, "Some aspects of non-stationary airfoil theory and its practical application," J. Aeronaut. Sci. **8**, 104–108 (1941).

[39] K. Streitlien, G. S. Triantafyllou, and M. S. Triantafyllou, "Efficient foil propulsion through vortex control," AIAA J. **34**, 2315–2319 (1996).

[40] S. Alben, "Passive and active bodies in vortex-street wakes," J. Fluid Mech. **642**, 95–125 (2010).

[41] J. C. Wu, "Theory for aerodynamic force and moment in viscous flow," AIAA J. **19**, 432–441 (1981).

[42] D. Paniccia, G. Graziani, C. Lugni, and R. Piva, "On the role of added mass and vorticity release for self-propelled aquatic locomotion," J. Fluid Mech. **918**, A45 (2021).

[43] D. Paniccia, G. Graziani, C. Lugni, and R. Piva, "The relevance of recoil and free swimming in aquatic locomotion," J. Fluid Struct. **103**, 103290 (2021).

[44] A. J. Smits, "Undulatory and oscillatory swimming," J. Fluid Mech. **874**, P1 (2019).

[45] J. Z. Wu, X.-Y. Lu, and L. X. Zhuang, "Integral force acting on a body due to local flow structures," J. Fluid Mech. **576**, 265–286 (2007).

[46] J. Z. Wu, H. Y. Ma, and M. D. Zhou, *Vortical Flows* (Springer, 2015).

[47] G. J. Li and X.-Y. Lu, "Force and power of flapping plates in a fluid," J. Fluid Mech. **712**, 598–613 (2012).

[48] L. L. Kang, L. Q. Liu, W. D. Su, and J. Z. Wu, "Minimum-domain impulse theory for unsteady aerodynamic force," Phys. Fluids **30**, 016107 (2018).

[49] B. S. H. Connell and D. K. P. Yue, "Flapping dynamics of a flag in a uniform stream," J. Fluid Mech. **581**, 33–67 (2007).

[50] R.-N. Hua, L. D. Zhu, and X.-Y. Lu, "Locomotion of a flapping flexible plate," Phys. Fluids **25**, 121901 (2013).

[51] S. Y. Chen and G. D. Doolen, "Lattice Boltzmann method for fluid flows," Annu. Rev. Fluid Mech. **30**, 329–329 (1998).

[52] R.-N. Hua, L. D. Zhu, and X.-Y. Lu, "Dynamics of fluid flow over a circular flexible plate," J. Fluid Mech. **759**, 56–72 (2014).

[53] C. S. Peskin, "The immersed boundary method," Acta Numer. **11**, 479–517 (2002).

[54] G. Taylor, R. Nudds, and A. Thomas, "Flying and swimming animals cruise at a Strouhal number tuned for high power efficiency," Nature **425**, 707–711 (2003).

[55] R. Mittal and G. Iaccarino, "Immersed boundary methods," Annu. Rev. Fluid Mech. **37**, 239–261 (2005).

[56] M. J. Lighthill, *An Informal Introduction to Theoretical Fluid Mechanics* (Clarendon Press, Oxford, 1986).